RAA 2019 Vol. **19** No. **5**, 66(12pp) doi: 10.1088/1674–4527/19/5/66
© 2019 National Astronomical Observatories, CAS and IOP Publishing Ltd.
http://www.raa-journal.org *http://iopscience.iop.org/raa*

***R**esearch in*
***A**stronomy and*
***A**strophysics*

Retrieving volume FeO and TiO_2 abundances of lunar regolith with *CE-2* CELMS data using BPNN method ⋆

Cai Liu[1,2,3], Hong-Yan Sun[1], Zhi-Guo Meng[1,2,3⋆⋆], Yong-Chun Zheng[3], Yu Lu[4,5], Zhan-Chuan Cai[2], Jin-Song Ping[3], Alexander Gusev[6] and Shuo Hu[1,2]

[1] College of Geoexploration Science and Technology, Jilin University, Changchun 130026, China; *mengzg@jlu.edu.cn*
[2] State Key Laboratory of Lunar and Planetary Sciences, Macau University of Science and Technology, Macau, China
[3] Key Laboratory of Lunar and Deep Space Exploration, National Astronomical Observatories, Chinese Academy of Sciences, Beijing 100101, China
[4] School of Geography and Ocean Science, Nanjing University, Nanjing 210023, China
[5] Jiangsu Center for Collaborative Innovation in Geographical Information Resource Development and Application, Nanjing 210023, China
[6] Institute of Geology, Kazan Federal University, Kazan 420008, Russia

Received 2018 October 18; accepted 2019 February 28

Abstract The volume FeO and TiO_2 abundances (FTAs) of lunar regolith can be more important for understanding the geological evolution of the Moon compared to the optical and gamma-ray results. In this paper, the volume FTAs are retrieved with microwave sounder (CELMS) data from the *Chang'E-2* satellite using the back propagation neural network (BPNN) method. Firstly, a three-layered BPNN network with five-dimensional input is constructed by taking nonlinearity into account. Then, the brightness temperature (T_B) and surface slope are set as the inputs and the volume FTAs are set as the outputs of the BPNN network. Thereafter, the BPNN network is trained with the corresponding parameters collected from *Apollo*, *Luna*, and *Surveyor* missions. Finally, the volume FTAs are retrieved with the trained BPNN network using the four-channel T_B derived from the CELMS data and the surface slope estimated from Lunar Orbiter Laser Altimeter (LOLA) data. The rationality of the retrieved FTAs is verified by comparing with the *Clementine* UV-VIS results and *Lunar Prospector* (*LP*) GRS results. The retrieved volume FTAs enable us to re-evaluate the geological features of the lunar surface. Several important results are as follows. Firstly, very-low-Ti ($<$1.5 wt.%) basalts are the most spatially abundant, and the surfaces with $TiO_2 > 5$ wt.% constitute less than 10% of the maria. Also, two linear relationships occur between the FeO abundance (FA) and the TiO_2 abundance before and after the threshold, 16 wt.% for FA. Secondly, a new perspective on mare volcanism is derived with the volume FTAs in several important mare basins, although this conclusion should be verified with more sources of data. Thirdly, FTAs in the lunar regolith change with depth to the uppermost surface, and the change is complex over the lunar surface. Finally, the distribution of volume FTAs hints that the highlands crust is probably homogeneous, at least in terms of the microwave thermophysical parameters.

Key words: planetary systems — Moon — evolution — imaging spectroscopy — data analysis

1 INTRODUCTION

The FeO and TiO_2 abundances (FTAs) of the Moon are fundamentally significant for understanding its origin and geological evolution, so that the measurement of FTAs on a global scale is always an important scientific objective for current lunar exploration (Neal 2009; Wu 2012).

The FTAs are two compositions that show special spectral features in visible (VIS) and near-infrared (NIR) ranges, which makes them be accurately identifiable in the field of remote sensing (Neal 2009; Wu 2012; Wu et al. 2012). Currently, FTAs have been successfully derived

⋆ A contributed paper of the International Symposium on Lunar and Planetary Science (ISLPS) on 2018 June 12–15 at Macau University of Science and Technology.

⋆⋆ Corresponding author.

from measurements in the VIS-NIR wavelength range. The method developed by Lucey et al. (1998, 2000) is widely accepted to retrieve FTAs with *Clementine* ultraviolet (UV)-VIS data. Gillis et al. (2004) improved Lucey's method and developed a dual-regression method to better estimate the TiO_2 abundance (TA) inversion. Additionally, Shkuratov et al. (1999) mapped the FTAs on the lunar nearside using Earth-based telescopic albedo data. Thereafter, data from the *KAGUYA* Spectral Profile (Matsunaga et al. 2008), *Chandrayaan-1* Moon Mineralogy Mapper (M^3) (Pieters et al. 2009) and *Chang'E* Interference Imaging Spectrometer (IIM) (Wu 2012; Wu et al. 2012; Yan et al. 2012) were also extensively employed to map the FTAs of the Moon with relatively better spatial or spectral resolution.

However, the inversion of the FTAs was doubted by Pieters et al. (2008) through analyzing the relationship between composition and reflectance spectrum of lunar mare regolith. This is also the reason that the retrieved FTAs are not widely used in lunar science (Pieters et al. 2008; Jiang & Jin 2011). Moreover, the inverted FTAs with optical data have poor penetration capabilities, which is only about a few microns deep in the uppermost lunar regolith (Fa & Wieczorek 2012; Meng et al. 2014). Morgan et al. (2016) and Meng et al. (2018a) demonstrated the great difference in regolith compositions with depth to the superficial layer postulated by Hiesinger et al. (2000) in Mare Imbrium. Thus, to better understand geological features of the Moon, volume FTAs at a certain depth will be more interesting than those in the superficial layer indicated by the optical data.

To obtain FTAs within a certain depth of lunar regolith, Gamma-Ray Spectrometer (GRS) data from *Lunar Prospector* (*LP*) were used, and the penetration depth of the data could be up to several tens of centimeters (Lawrence et al. 1998; Elphic et al. 2000; Feldman et al. 2002; Prettyman et al. 2006). The results show apparent differences from the aforementioned retrievals. However, the spatial resolution of the GRS data is rather poor, which severely restricts extensive applications of the inverted volume FTAs. Therefore, to get the FTAs of lunar regolith to a certain depth with a proper spatial resolution is essential to current lunar study.

In the Chinese lunar exploration program, a microwave sounder (CELMS) was aboard the *Chang'E* (*CE*) satellites with the purpose of measuring the brightness temperature of lunar regolith. The penetration depth of CELMS data can be up to several meters (Wang et al. 2010; Jiang & Jin 2011; Meng et al. 2014; Pabari 2016), and the spatial resolution is better than that of *LP* GRS data. Chan et al. (2010), Zheng et al. (2012), Meng et al. (2016, 2018a) and Hu et al. (2018) demonstrated the strong correlation between CELMS data and FTAs based on observations and the theoretical model using a radiative transfer model. Therefore, the CELMS data provide the best candidate for evaluating the volume FTAs of lunar regolith.

However, the CELMS data are hardly used to retrieve the volume FTAs of lunar regolith directly with the theoretical model for the following reasons. Firstly, the theoretical model requires critical lunar regolith parameters, including the temperature profile, dielectric constant, particle size, buried rocks and surface roughness. Unfortunately, knowledge about such parameters is rarely sufficient (England 1975; Keihm 1984; Jiang et al. 2008; Fa & Wieczorek 2012; Meng et al. 2014). Secondly, the inversion of FTAs with the theoretical model is related to the solution of nonlinear integral-differential radiative transfer equations, which may likely lead to 'ill-posed' problems (Keihm 1984; Fa & Wieczorek 2012; Meng et al. 2014). So, how to avoid the influence from the aforementioned disadvantages of the theoretical model and provide an efficient way to extract the volume FTAs from lunar regolith still remain crucial problems in current lunar research.

As an excellent nonlinear fit theory, the back propagation neural network (BPNN) method has been widely used in information extraction, target identification and biomedical engineering (Montopoli et al. 2011; Li et al. 2012; Meng et al. 2014). With BPNN methodology, Montopoli et al. (2011), Li et al. (2012) and Meng et al. (2014) successfully evaluated certain regolith parameters over the lunar surface. This makes the BPNN method an appealing candidate to estimate the FTAs of lunar regolith. In this paper, the BPNN method is selected as an attempt to invert the volume FTAs of lunar regolith using CELMS data from the *CE-2* lunar orbiter. In Section 2, the architecture of the BPNN network and the training procedure are described. Additionally, CELMS data and Lunar Orbiter Laser Altimeter (LOLA) data are processed to obtain the brightness temperature (T_B) and surface slope, respectively. Then the volume FTAs of lunar regolith are retrieved using the BPNN method as shown in Section 3. The rationality of the inverted FTAs is also analyzed. Section 4 presents several important implications of the retrieved FTAs. The conclusions are drawn in Section 5.

2 METHODOLOGY

2.1 BPNN Construction and Training

BPNN resembles a human brain in that the model learns and stores knowledge (Mehra & Wah 1992), which comprises several idealized layers of nodes and is specified by the weights, learning rules, network interconnection geom-

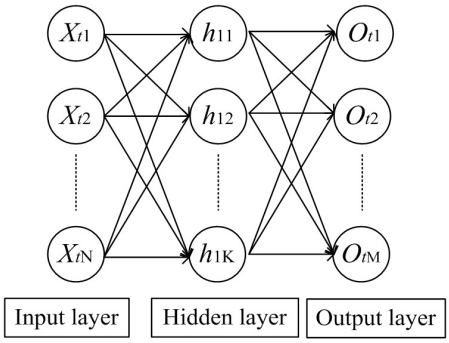

Fig. 1 Structure of a three-layer BPNN network.

etry and dimensionality. Because BPNN takes nonlinearity into account using sigmoid functions that connect the BPNN layers of nodes, the errors can be significantly decreased through the back propagation learning process.

The construction of a BPNN network has been thoroughly described in many literatures (Lippmann 1987; Rumelhart & McClelland 1987; Montopoli et al. 2011; Li et al. 2012; Meng et al. 2014). Considering the close correlation between CELMS data and the volume FTAs, one hidden layer of nodes is applied in this study. Thus, a three-layer neural network algorithm is constructed: one input layer, one hidden layer and one output layer (Fig. 1). Note that the input, X_{t_j} $(t = 1, 2, ..., T;\ j = 1, 2, ..., N)$, is the jth parameter of the tth sample, and N is the number of specified parameters for every input sample; and the output, O_{t_s} $(t = 1, 2, ..., T;\ s = 1, 2, ..., M)$, is the sth parameter of the corresponding tth sample, and M is the number of given parameters for every output sample. T is the total number of sets of the available samples for network training.

According to the simulation results, the relationship between T_B and volume FTAs is highly influenced by the surface slope θ (Fa & Wieczorek 2012; Meng et al. 2014; Meng et al. 2016; Hu et al. 2018). Onboard the *CE-2* lunar orbiter, the CELMS instrument operated at four channels. Therefore, the four-channel T_B derived from *CE-2* CELMS data and θ estimated with LOLA data are selected as the input parameters to construct the BPNN network.

Therefore, for the input X_{t_j} $(t = 1, 2, ..., T;\ j = 1, 2, ..., N)$, T_{B_i} $(i = 1, ..., 4)$ and θ are input parameters, and N is 5. Regarding the output O_{t_s} $(t = 1, 2, ..., T;\ s = 1, 2, ..., M)$, the FTAs are set as the output of the BPNN network and the dimension of the output layer M is 2. Moreover, due to the absence of lunar regolith samples, only the regolith parameters for *Apollo*, *Luna* and *Surveyor* landing sites are available to train the BPNN network. Thus, the total number of available samples, T, is 12 (Table 1). Here, the used FTAs were measured during the *Apollo* (A), *Luna* (L) and *Surveyor* (S) missions, which are regarded as the volume values.

Thereafter, the Generalized Delta Rule is used to train the three-layer BPNN network. The first layer distributes input parameters selected from the previous analysis. Values of the nodes in the hidden layer are the summation of each input parameter multiplied by its connection's weights to the corresponding nodes. Each node in the third layer receives output from the node in the second layer, at which time it is processed through a function and weighted again. The training process and weights are determined separately for each training pair using the sigmoid function, which enables the network to model nonlinear problems (Li et al. 2012; Meng et al. 2014).

The goal of the training process is to optimize weights for every node by minimizing the difference between the actual network output and the measurements. The BPNN changes the weights of all nodes in the middle layer through the feedback process to minimize average error (E) of the system. When E reaches a minimum threshold, or the total number of iterations reaches a limited time, the training process for the BPNN is completed.

Originally, 12 training pairs from *Apollo*, *Luna* and *Surveyor* landing sites were available to train the BPNN network. However, the amount of training examples is severely insufficient. To increase the quantity of BPNN training samples, the 12 training pairs are used ten times or more, which is equivalent to 120 or more training pairs. Moreover, according to the training results, the number of neurons at the hidden layer is set to 9, the predetermined threshold is set to 5% of the average measurements and the total number of iterations is set to 1000. Once trained, all the node weights are optimized and the BPNN model is ready for predicting the FTAs with the new input parameters, including four-channel T_B data and θ.

2.2 CELMS Data Processing

The *CE-2* lunar orbiter was launched successfully on 2010 October 1, and finished its observations on 2011 June 9. The orbital altitude was about 100 km. The CELMS instrument was used to investigate the T_B of lunar regolith, which operated at 3.0, 7.8, 19.35 and 37.0 GHz. The observation angle was 0° (Cai & Lan 2017; Meng et al. 2017). In this study, Level 2C swath data are used, which are the raw data processed after geometric correction and radiometric calibration. Their archive format is Planetary Data System (PDS). As a single file, the level 2C data contain a header and a table of measured data, which comprise the observation time, four-channel T_Bs, solar incidence angle and azimuth angle, selenographic latitude and longitude,

Table 1 Regolith Parameters at *Apollo* (A), *Luna* (L) and *Surveyor* (S) Landing Sites (Shkuratov et al. 1999)

Location	Lat.(°)	Long.(°)	Input parameter					Output parameter	
			3 GHz	7.8 GHz	19.35 GHz	37 GHz	θ	FeO	TiO_2
A11(X1)	0.7N	24.3E	237.32	242.2	259.67	275.64	0.55	0.158	0.074
A12(X2)	3.2S	23.4W	234.56	240.23	256.64	272.40	0.60	0.157	0.0268
A14(X3)	3.7S	17.5W	233.79	236.75	257.30	272.92	0.58	0.104	0.0164
A15(X4)	26.1N	3.7E	228.54	223.35	248.72	264.03	0.62	0.152	0.0164
A16(X5)	9.0S	15.5E	234.99	231.91	254.58	268.10	0.64	0.05	0.0055
A17(X6)	20.2N	30.8E	232.41	228.06	252.94	268.62	0.67	0.15	0.095
L16(X7)	0.68S	56.30E	239.48	242.40	263.75	280.97	0.53	0.167	0.0336
L20(X8)	3.57N	56.50E	240.36	233.64	263.50	281.55	0.61	0.074	0.0047
L24(X9)	12.25N	62.20E	233.68	235.11	260.06	276.27	0.62	0.206	0.0115
S5(X10)	1.41N	23.18E	238.10	244.37	261.41	278.21	0.58	0.121	0.076
S6(X11)	0.46N	1.37W	236.59	238.55	258.52	274.84	0.69	0.124	0.035
S7(X12)	41.01S	11.41W	212.54	208.16	228.69	239.76	1.22	0.055	0.05

Notes: The data in columns for 3.0 GHz, 7.8 GHz, 19.35 GHz and 37 GHz are selected for T_B at noontime.

and so on (Fang & Fa 2014; Meng et al. 2016). According to prelaunch calibration experiments, the radiometric accuracy is better than 1.0 K depending on temperature and frequency.

The nominal spatial resolution is 15 km for channels corresponding to 7.8, 19.35 and 37.0 GHz, and is 25 km for 3.0 GHz (Cai & Lan 2017; Meng et al. 2019). But after overlying the obtained CELMS data on the lunar surface (Fig. 2), 1° spatial resolution along latitude and very high spatial resolution along longitude are clearly present. Therefore, 1°×1° is a proper spatial resolution to generate the global T_B maps, and the fitting scheme used is a seven-degree polynomial method. Moreover, through comparison of the CELMS data and the FTAs obtained with *Clementine* UV-VIS data, Chan et al. (2010), Zheng et al. (2012) and Meng et al. (2018a) demonstrated that the T_B at noon shows strong correlation with FTAs. Therefore, only the T_B at noon is employed in this study.

We note that the value of T_{B_i} ($i = 1, ..., 4$) ranges from 100 K to about 300 K, but this is not acceptable for obtaining a good result using the BPNN method with a sigmoid function (Elphic et al. 2000; Li et al. 2012). Therefore, the T_B needs to be normalized, in the form nT_B, with Equation (1)

$$nT_{B_i} = \frac{(T_{B_i}(m,n) - \min(T_{B_i}(:,n)))}{(\max(T_{B_i}(:,n)) - \min(T_{B_i}(:,n)))}\ , \qquad (1)$$

where (m, n) is the position of the study point, the range of m is (1, 2, ..., 360) and n is (1, 2, ..., 180). i is (1, 2, 3, 4) and T_{B_i} represents one channel in the four-channel CELMS data. $T_{B_i}(:, n)$ is the data series in the nth line. $\max(T_{B_i}(:, n))$ is the maximum of $T_{B_i}(:, n)$ and $\min(T_{B_i}(:, n))$ is the minimum one. Figure 3 is the nT_B map at 37 GHz, whose range is scaled from 0 to 1.

2.3 LOLA Data Processing

On a macroscale, θ may alter the effective solar illumination of the lunar surface, which indirectly changes the microwave thermal emission of lunar regolith (He et al. 2013; Meng et al. 2014; Hu et al. 2018). Therefore, according to the method provided by Rosenburg et al. (2011), the distribution of θ was estimated by LOLA data from the Lunar Reconnaissance Orbiter (LRO) satellite. The LOLA data were acquired from 2009 September 17 to 2010 March 9, which were downloaded from `http://pds-geosciences.wustl.edu/`. Considering the spatial resolution of T_B maps, the mean θ in one CELMS pixel is employed as the new lunar surface parameter. Additionally, the range for θ is from 0° to about 25°, which is normalized with Equation (2)

$$n\theta = \frac{(\theta(m,n) - \min(\theta(:,n)))}{(\max(\theta(:,n)) - \min(\theta(:,n)))}\ , \qquad (2)$$

where $n\theta$ is the normalized θ. $\theta(:, n)$ is the data series in the nth line. $\max(\theta(:, n))$ is the maximum of the $\theta(:, n)$ and $\min(\theta(:, n))$ is the minimum one.

Figure 4 is the $n\theta$ map, whose range is from 0 to 1.

Additionally, the azimuth of θ is also important in impacting the T_B of lunar regolith (Meng et al. 2014; Hu et al. 2018). There are two reasons for us to neglect the parameter. Firstly, the observation angle of the CELMS instrument is 0°, so that the influence of azimuth is weakened to some extent. Secondly, surface topography plays a weak role in the T_B in middle and low latitude regions, which has been demonstrated by comparative studies in the Hertzsprung basin and Mare Imbrium (Meng et al. 2018a,c).

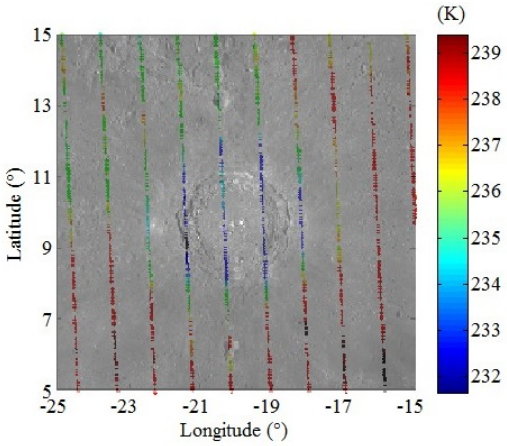

Fig. 2 Scatter map of the CELMS data at noon targeting Copernicus crater (Meng et al. 2019).

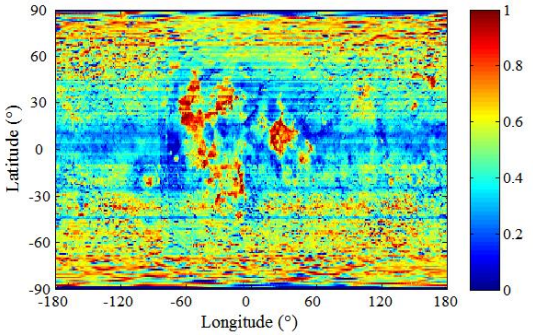

Fig. 3 Distribution of nT_B over the lunar surface, 37 GHz, at noon.

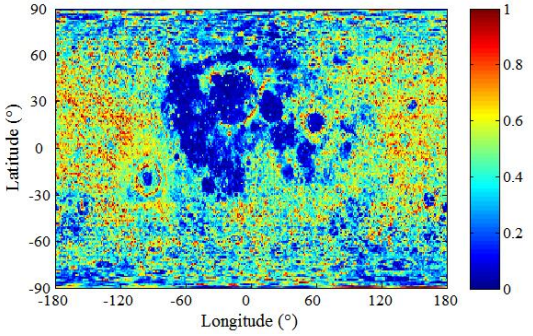

Fig. 4 Distribution of the normalized θ.

3 FTA RETRIEVAL

In this section, the volume FTAs of lunar regolith are retrieved and evaluated with those estimated with GRS data and UV-VIS data.

3.1 Retrieval of FTAs

Employing the trained BPNN network, for any given set of input parameters, the BPNN will rapidly generate a series of output values $O = [O_1 O_2]^T$. Here, O_1 is the volume FeO abundance (FA), and O_2 is volume TiO_2 abundance. Through this way, the volume FTAs of lunar regolith (Fig. 5) can be efficiently retrieved using the generated nT_B and $n\theta$ in the previous section.

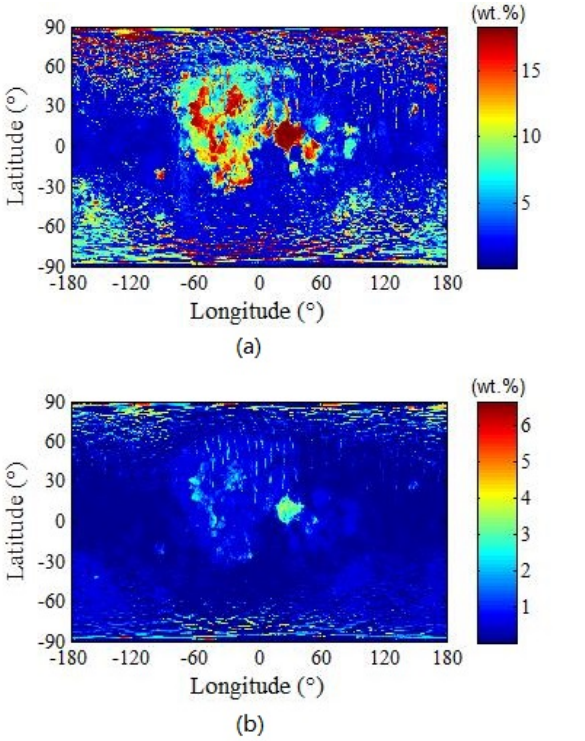

Fig. 5 Mapping of the volume FeO (a) and TiO_2 (b) abundances with CELMS data using the BPNN method.

Figure 5 shows that the retrieved FTAs in maria are much higher than those in highlands, and the inverted FA is apparently much higher than the TA, which agree with current knowledge about the surface FTA distribution on the Moon. Secondly, the FA in maria varies widely from about 5 to 18 (wt.%) and the TA changes from about 2 to 6 (wt.%), while the FTAs in highlands are rather low, which is largely less than 5 wt.% of FA and 2 wt.% of TA. This is much lower than those estimated with the spectral and GRS data. Interestingly, Korokhin et al. (2008) employed a nonlinear analysis of *Clementine* UV-VIS data and Lunar Soil Characterization Consortium (LSCC) data to prognosticate the TA in lunar soil, and they concluded that TA in highlands is less than 2%. Similar results were also suggested by Wu et al. (2012) and Wu (2012) using the *CE-1* IIM data. This coincides well with our results, hinting that the retrieved FTAs are rational and the BPNN method is feasible for evaluating FTAs with the CELMS data.

However, two phenomena should be mentioned in Figure 4. Firstly, there are abundant belts in the northern hemisphere. This may have resulted from the CELMS data used, because the CELMS data could not cover the whole surface of the Moon at a specific time and the data in the

belts are fitted but not measured values (Chan et al. 2010; Zheng et al. 2012). Secondly, the retrieved FTAs are abnormally large in high latitude regions. The main cause for such a phenomenon might be that the sampled parameters are collected from *Apollo*, *Luna* and *Surveyor* landing sites, which are all in the low and middle latitude regions. Hence, the BPNN method is not suitable for FTA evaluation in high latitude regions due to the limitation of sampling positions.

3.2 Rational Analysis

Validation of the retrieved parameters in the field of remote sensing is highly dependent on the "Ground Truth" Data. Until now, FTAs have successfully been evaluated with *Clementine* UV-VIS data (Lucey et al. 1998, 2000; Gillis et al. 2004), *CE* IIM data (Wu 2012; Wu et al. 2012; Yan et al. 2012), and *LP* GRS data (Lawrence et al. 1998; Prettyman et al. 2006). In this study, the FTAs evaluated with *Clementine* UV-VIS data (Fig. 6) (Gillis et al. 2004) and *LP* GRS data (Fig. 7) (Prettyman et al. 2006) are employed as the "Ground Truth" to evaluate the inverted FTAs. Also, the inverted FTAs with *CE* IIM data are introduced for reference.

3.2.1 Comparison with Clementine FTAs

Generally, direct comparison between CELMS FTAs and *Clementine* FTAs gives overall similarity. Firstly, very low FTAs exist in the highlands, while high FTAs occur in the mare and several large basins. Secondly, the relatively higher FA are both found in Maria Tranquillitatis, Fecunditatis, Humorum, Vaporum, Imbrium and Oceanus Procellarum, while the high TA mainly exists in Maria Tranquillitatis, Imbrium and Oceanus Procellarum.

On a local scale, Figures 5 and 6 both demonstrate that the relatively higher FTAs appear in the middle of Oceanus Procellarum, western part of Mare Imbrium, southeastern part of Mare Vaporum and eastern part of Mare Nubium. Also, the FTAs in the southern part of Orientale basin are higher than those in the northern part. Particularly, the FTAs in Apollo basin (36.1°S, 151.8°W) are obviously higher than in the nearby regions. In Mare Australe, the distribution of regions with high FA from CELMS results is highly consistent with that of *Clementine*. Also, the *Clementine* FTAs and CELMS FTAs indicate a small patch with very low values surrounding Struve crater (23.0°N, 76.6°W), in the northwestern part of Oceanus Procellarum.

Therefore, our results are rational on local and global scales compared to the *Clementine* FTAs.

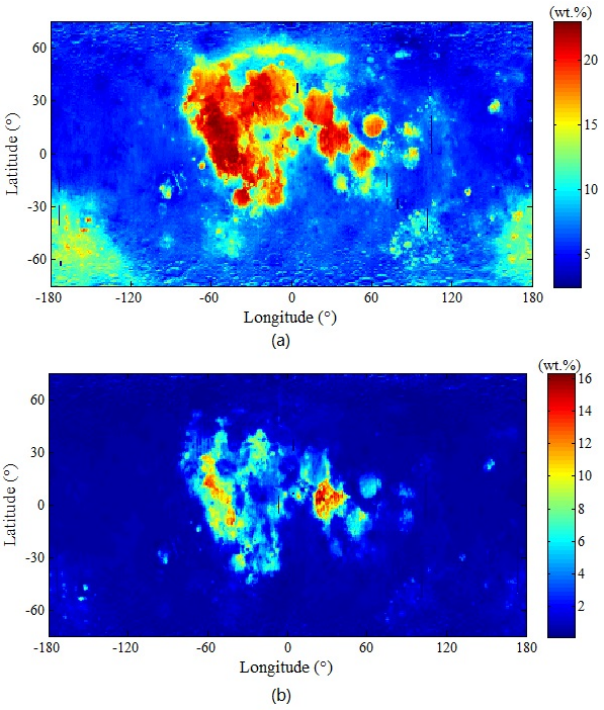

Fig. 6 Mapping of the FeO (a) and TiO_2 (b) abundances with the *Clementine* UV-VIS data using the improved Lucey method (Gillis et al. 2004).

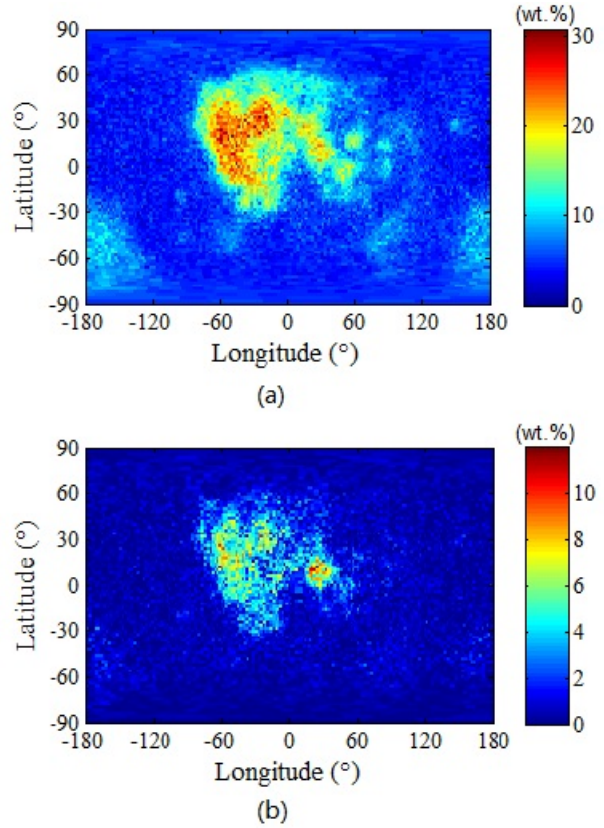

Fig. 7 Mapping of the FeO (a) and TiO_2 (b) abundances with the *LP* GRS data (Prettyman et al. 2006).

3.2.2 Comparison with LP GRS elemental abundances

Figure 7 shows the FTA maps determined by *LP* GRS data (Prettyman et al. 2006). However, due to the low spatial resolution of GRS data, a detailed comparison between the *LP* GRS results and CELMS results can hardly be obtained. Besides the coincidence related to global distribution of the two results, they also postulate a good agreement between Mare Imbrium and Oceanus Procellarum on a regional scale.

Interestingly, in some mare areas, such as Maria Serenitatis, Fecunditatis, Moscoviense and Crisium, *LP* GRS and CELMS TAs are similarly low. Especially in Mare Crisium, *LP* GRS TA and CELMS TA both present very low values, which were supported by measurements of the *Luna 24* sample (Lawrence et al. 2002; Elphic et al. 2002). These distributions are apparently different from the *Clementine* results. Moreover, in Mare Tranquillitatis, the CELMS FA agrees well with the *Clementine* and *LP* GRS results, while the *LP* GRS TA and CELMS TA are higher in the north basin floor than that in the south, different from *Clementine* TA. Moreover, the CELMS TA is nearly the same as that of the *LP* GRS TA. The CELMS TA has a range of up to about 7 wt.%, and the *LP* GRS TA in the most extensive regions does not go above 8 wt.% (Lawrence et al. 2002), which are both apparently less than the *Clementine* TA.

Our results also show a good coincidence with the *CE* IIM results from Wu et al. (2012), not only in the data range but also in the following typical regions. The first region is in Mare Serenitatis and Mare Tranquillitatis, where *Clementine* FA in the former is similar to that in the latter. However, the CELMS and IIM FAs in Mare Serenitatis are both much lower than those in Mare Tranquillitatis. The second region is in Maria Moscoviense and Orientale. CELMS and IIM results both indicate a considerably high FA value like that in the western part of Mare Imbrium, while *Clementine* results show a rather low FA value.

Generally, the retrieved FTAs are fairly close to those obtained with the three datasets in terms of spatial distributions and they coincide well with *LP* GRS and *CE*-IIM FTAs in terms of values. The comparison not only validates that the estimated FTAs with CELMS data are rational, but also suggests a difference of the four results in understanding the lunar geological features.

4 GEOLOGICAL SIGNIFICANCES

The global maps of FA and TA derived from CELMS data enable us to re-evaluate the statistical characteristics of FeO and TiO_2, their relationship across the Moon and the geological features of the lunar surface.

4.1 New Views about FTA Distributions

Statistical analysis shows that the surfaces with TA $>$ 5 wt.% constitute less than 10% of the maria, while very-low-Ti ($<$ 1.5%) basalts are the most spatially abundant and high-Ti basalts are the least abundant. This is comparable to the *LP* GRS and *CE* IIM results, but it is very different from the *Clementine* results. Lucey et al. (2000) found that mare surfaces with TA $>$ 5 wt.% constitute only 20% of the maria. Moreover, the TA derived by Lucey et al. (2000) and Wu et al. (2012) shows that the farside maria are dominated by very-low-Ti basalts, but the CELMS results indicate a relatively higher TA on the farside, particularly in Mare Moscoviense and the southwestern part of Apollo basin.

Figure 8 shows histograms of the FTAs for the entire CELMS data set, which display several aspects that are different from the previous results (Lucey et al. 2000; Prettyman et al. 2006; Wu et al. 2012). The first aspect is the shapes of the the FA and TA histograms. The histogram of FA has three peaks, where the first and second highest peaks both correspond to mare and the lowest one is related to highlands. The histogram of the TA is a unimodal continuum distribution. Secondly, the lowest FA peak of about 2.26 wt.% is apparently lower than the *Clementine* peak abundance given by Lucey et al. (1998) and Gillis et al. (2004). Interestingly, the highest FA peak is close to the average *LP* GRS abundance given by Prettyman et al. (2006) and the M^3 abundance provided by Zhang & Bowles (2013). Moreover, the TA peak indicated by the histogram is much lower than that given by Lucey et al. (2000), while it is similar to the IIM peak abundance given by Wu et al. (2012); Wu (2012) if the largest and lowest peaks are omitted, which are mainly caused by the topography. Similar to the FA peak, the highest average TA determined in this study is found in Mare Tranquillitatis, about 4.03 wt.%, which is comparable to the results determined by Zhang & Bowles (2013) and Korokhin et al. (2008).

The data from the lunar samples indicate that TA displays a complex relationship with FA in mare basalt (Heiken et al. 1991; Wu et al. 2012). With the FTAs estimated with IIM data, Wu et al. (2012) thought that the relationship between FA and TA exhibits a form that slightly resembles an obtuse triangle covering an area similar to where returned samples were collected.

Figure 9 depicts the scatterplot of FA and TA estimated with the CELMS data, which indicates a steep, well-defined increase with FA for the regions with high TA. Two features in Figure 8 should be noticed. Firstly, although the relationship between FA and TA is nonlinear, this correlation is apparently better than that indicated by the opti-

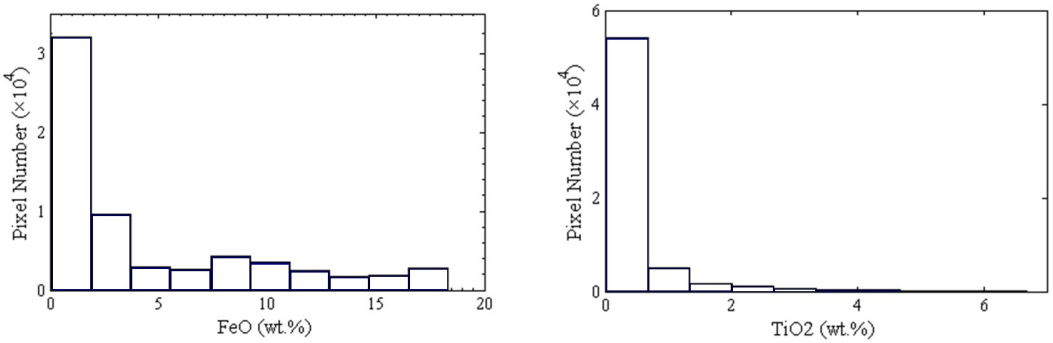

Fig. 8 Histograms of FA (a) and TA (b) for the lunar surface.

cal results. Secondly, the relationships between FA and TA are obviously linear before and after the threshold, about 16 wt.% for FA. The two linear relationships may hint at a different view regarding mare volcanism over the lunar surface.

4.2 A New View about Mare Volcanism

What we know about mare volcanism is mainly from the distribution of FTAs over the lunar surface. Compared to the optical results, Figure 5 indicates a new view about mare volcanism represented by the following several regions.

Firstly, in Oceanus Procellarum, Figure 5 shows that the regions with high FTAs mainly exist in the middle part along latitude and they extend as a broad belt region from north to south. Interestingly, this distribution can be partly supported by the *Clementine* TA distribution in Figure 6(b). Additionally, the optical results indicate that the belt region is not continuous, while the CELMS FTAs manifest a continuous belt region with high values. The difference between the *Clementine* results and CELMS results is probably from contamination of the impact ejecta from other regions, which plays an important role in the measured optical data (Lucey et al. 1998; Wu et al. 2012). After all, Aristarchus, Copernicus and Kepler craters are located not far from the belt, and even the ejecta from Tycho crater at a far distance also altered the surface compositions to some extent (Desai et al. 2014). Moreover, Adams et al. (1978); Haruyama et al. (2009) suggested that higher FTAs mostly appear in younger basalts. Considering the relationship between the age and FTAs, such phenomenon implies the existence of the last stage of mare basalts in Oceanus Procellarum, which also gives some clues when looking for the sources of mare basalts.

Secondly, in Mare Crisium, Figure 5 postulates a different view compared to the *Clementine* FTAs. Figure 6(a) shows that most of Crisium basin is filled with high-FA basalt, while Figure 6(b) displays high TA values in the southeastern basin floor. That is, the agreement between FA and TA in the basin is not good. Considering the abundance of large craters, such as Peirce (53.4°E, 18.3°N) and Picard (54.7°E, 14.6°N) inside the basin and Proclus Proclus (46.9°E, 16.1°N) and Eimmart (64.8°E, 24.0°N) surrounding the basin, it is likely that crater ejecta changed the surface compositions of the lunar regolith. However, Adams et al. (1978), Spudis & Sliz (2016) and Spudis & Sliz (2017) described their understanding about the geological units in Mare Crisium, and the interpreted results are greatly different from each other.

Compared to the optical results in Figures 6, Figure 5 demonstrates that the highest FTAs only exist in the most eastern portion of the basin floor, Alhazan unit. Moreover, the FTAs in the other parts of the basin floor are similar, which are higher than the nearby highlands but apparently lower than those in Alhazan unit. This indicates that the mare basalts in Crisium basin should only be divided into two stages, very different from the previous results (Adams et al. 1978; Spudis & Sliz 2016, 2017). Furthermore, Adams et al. (1978)) and Haruyama et al. (2009) suggested that the higher-FTA basalts mostly appear in younger basalts. Thus, the distribution features of the FTAs postulate that the last stage of mare basalt should exist in Alhazen unit and this is also the origin of lava for the whole Crisium basin. Thereafter, late impact events strongly alter the superficial layer of mare basalts. A similar conclusion is also obtained by directly analyzing the microwave thermal emission of mare basalts using the *CE-2* CELMS data and the *LRO* Wide Angle Camera (WAC) data (Meng et al. 2018b).

Thirdly, the retrieved FTAs in Mare Serentatis are also rather different from the *Clementine* results. Figure 6 indicates that the FA in Mare Serentatis is largely similar as that in Mare Tranquillitatis, while the TA in the former is much less than the latter. However, the CELMS results in Figure 5 show that both FA and TA in Mare Serentatis

are much less than those in Mare Tranquillitatis, especially the FA. Combined with the penetration features of the two datasets, this indicates that high FA only exists in the superficial layer of Mare Serentatis, and that FTAs in the deep layer penetrated by the CELMS data are low. Also, the *LP* GRS FTAs present low values in the mare, validating the rationality of our results. Additionally, the FTA values are lower than those in the eastern part of Mare Imbrium and they are nearly similarly low as those in the northern highlands. Therefore, the mare volcanism as identified with the *Clementine* FTAs should be re-examined with more sources of data in this field.

Last but most importantly, Giguere et al. (2000) demonstrate that maria on the lunar farside are dominated by very-low-Ti basalts according to *Clementine* results. However, Figure 5 indicates that the FTAs in several important regions such as Mare Moscoviense, Apollo basin and Tsiolkovskiy crater are much higher than those in the *Clementine* results. Moreover, the FTAs in the three mentioned regions are similarly high as those in the middle of Oceanus Procellarum and western part of Mare Imbrium, indicating relatively younger mare basalts on the lunar farside compared to those on the nearside. Such conclusion can also be verified by the findings of Adams et al. (1978); Haruyama et al. (2009); Pasckert et al. (2018), who suggest the existence of young mare basalts on the lunar farside with the crater size-frequency distribution method. Therefore, mare volcanism on the lunar farside should be re-investigated with more sources of data in the future. We also hope that these findings would be helpful to better use the in-situ data measured by the *CE-4 Yutu-2* rover.

4.3 Change of FTAs with Depth

The previous discussions indicate that the retrieved FTAs with CELMS are acceptable. Meanwhile, the FTAs estimated with *Clementine* UV-VIS (Gillis et al. 2004) and with *LP* GRS data (Prettyman et al. 2006) are widely accepted in current Moon research (Korokhin et al. 2008; Wu et al. 2012; Zhang & Bowles 2013). Considering the penetration depth of the UV-VIS signal, GRS signal and CELMS signal, Figures 6, 7 and 5 probably hint at the change of FTAs with depth in the lunar regolith.

The penetration depth of the UV-VIS signal is only several microns, the penetration depth of the GRS signal is up to 50 cm and the CELMS signal can penetrate the lunar regolith up to several meters (Jin et al. 2003; Fa & Wieczorek 2012). That is, Figure 6 depicts the FTAs of the uppermost lunar regolith, and Figure 7 represents the FTAs in several tens of centimeters of the lunar regolith, while Figure 5 is largely the average FTAs in several meters of the lunar regolith.

A comparison of Figures 6, 7 and 5 demonstrates the change of FTAs from the uppermost layer to a certain depth in lunar regolith. Figure 6 hints that the FTAs are largely high in Oceanus Procellarum, especially in the middle and southwestern parts. Whereas, Figure 7 indicates that the area with high FTAs is much less than those at Figure 6. Interestingly, Figure 5 signifies that only the middle of Oceanus Procellarum has high FTAs, which is largely similar to that in Figure 7. Moreover, in Mare Imbrium, the FTAs in the western part are a bit higher than those in the eastern part in Figure 6, while Figure 7 and Figure 5 both postulate that the FTAs in the western part are much higher than those in the eastern part. Also, in Mare Serenitatis, only Figure 6 shows that the FA is high here, whereas Figures 7 and 5 demonstrate that FA is rather low here. The aforementioned comparison indicates that the FTAs in lunar regolith at some depth are different from those in the uppermost surface.

Figure 10 is the FA (a) and TA (b) estimated with CELMS data (Curve 1, line in blue), *LP* GRS data (Curve 2, line in green) and *Clementine* UV-VIS data (Curve 3, line in red), which represent the average FTAs in the deep layer, upper layer and uppermost layer of the lunar regolith respectively.

Figure 10 hints that the change of FTAs with depth is complex. Generally, the FTA values estimated with UV-VIS data are the highest and those estimated with CELMS data are the lowest among the three kinds of dataset. That is, the FTAs are decreasing with depth. But, the FA in Sinus Aestuum (about 20°W to 5°W), Sinus Medii (about 5°W to 0°E), Mare Fecunditatis (about 44°E to 60°E) and Mare Smythii (about 80°E to 100°E) seemingly does not vary with depth, which suggests homogeneity of the lunar regolith in these places. From such a viewpoint, similar distribution features of FTAs in Mare Tranquillitatis, Nectaris and Humorum in Figures 5, 6, and 7 reveal that the lunar regolith is homogeneous there. Whereas in Mare Tranquillitais (about 19°E to 32°E), the FA is increasing with depth as hinted at by the three datasets. Such a phenomenon not only implies the complexity of the lunar regolith in the vertical direction, but also provides a new content which is worth further study in the future.

4.4 Homogeneity of Lunar Highlands Crust

Pieters (1993) and Tompkins & Pieters (1999) found that the lunar highlands crust below the surface is compositionally diverse by investigating the mineralogy of the central peaks, representing materials from a depth of 5 to 30 km.

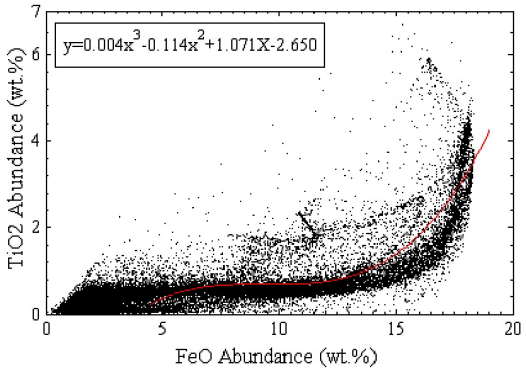

Fig. 9 Scatterplot of FA and TA for the whole lunar surface.

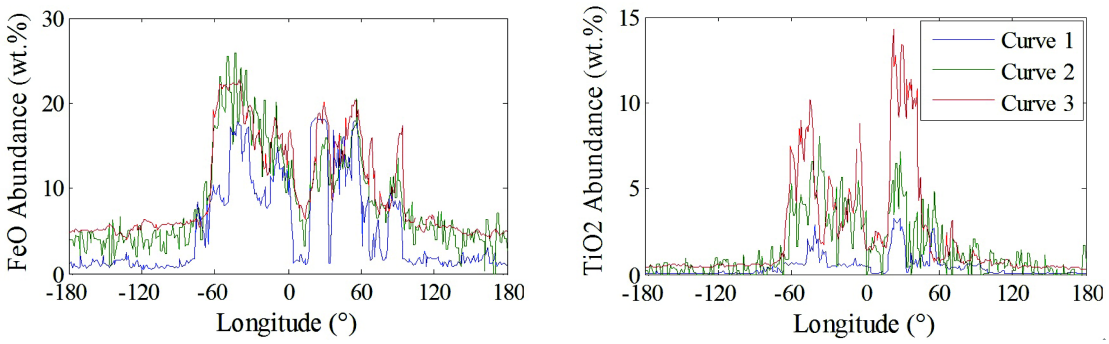

Fig. 10 Distribution of FeO (a) and TiO_2 (b) abundances along the Moon's equator. Curve 1: Estimated with CELMS data; Curve 2: Estimated with *LP* GRS data; Curve 3: Estimated with *Clementine* UV-VIS data.

Wu et al. (2012) studied the elemental abundance trends of the topmost surface of lunar highlands using high resolution FA and TA maps estimated with IIM data and concluded that the lunar highlands crust is relatively uniform on the quadrant scale but inhomogeneous on the global scale.

However, as mentioned above, the optical spectrum is strongly affected by impact ejecta, topography and other factors (Pieters 1999; Wu et al. 2012). That is, the conclusion from IIM data and UV-VIS data that the lunar highlands crust is inhomogeneous should be re-evaluated.

Figure 5 presents a distinctly different viewpoint about the compositional structure of highlands crust in the following several aspects. Firstly, nearly the whole lunar highlands are indicated by considerably low volume FTAs. This conclusion is also verified in part by the TA estimated by Korokhin et al. (2008) with *Clementine* data and by Wu (2012) with *CE-1* IIM data and the FTAs estimated by Prettyman et al. (2006) with *LP* GRS data and by Zhang & Bowles (2013) with M^3 data, which show that the low values are uniformly distributed on almost the whole highlands. Secondly, in the South Pole-Aitken (SPA) basin, the largest crater on the Moon, Figure 6 postulates that the *Clementine* FTAs in the whole basin are apparently higher than in the surrounding highlands, while Figures 5 and 7 indicate that the relatively higher volume FTAs only occur in several small patches, but not the whole basin. Additionally, the volume FTAs in the considered regions are nearly similarly low as those in highlands regions, especially in the wester part of Apollo basin and the western portion of the SPA basin. Thirdly, the FTAs around the typically large highlands craters are similar. Particularly in Hertzsprung basin (2°N, 128°W) with a diameter of 570 km, it excavated the lunar crust as deep as 40 km below the surface (Meng et al. 2018c). Changes in FTAs do not occur from the basin center to a far distance. Thus, the shallow lunar highlands crust is likely homogeneous at least in microwave thermophysical parameters.

What gets us in trouble is the the FA between Mare Imbrium and Mare Frigoris, which is much higher than that in other highlands places in Figure 5. This phenomenon is also pointed out by Wu et al. (2018) using both M^3 and *CE* IIM data. This means that the high FA values in the region are not only on the surface layer, but also in the deep layer. Also, considering the ubiquitous low-calcium pyroxene and large amounts of olivine surrounding the Imbrium distribution, Wu et al. (2018) speculated about the change in composition with depth in the lunar crust. This puts our

conclusion about the homogeneity of the highlands crust in doubt. Even though, the CELMS FTAs postulate a different view about the composition distribution of the shallow lunar crust compared to the VIS results.

5 CONCLUSIONS

In the lunar mare volcanism study, the volume FTAs of lunar regolith are more meaningful compared to the optical results. The measured CELMS data provide a potential way to evaluate the volume regolith FTAs for the lunar surface.

In this study, new global maps of the volume FTAs are derived with the CELMS data from the *CE-2* satellite. Firstly, the three-layer BPNN technique is constructed to retrieve the FTAs of lunar regolith. With the T_B data generated with CELMS data, surface slope estimated from LOLA data and the corresponding FTAs obtained during the *Apollo*, *Luna* and *Surveyor* missions, the volume FTAs of lunar regolith are retrieved with the BPNN method. Comparisons of the inverted volume FTAs to those estimated with *Clementine* UV-VIS data and *LP* GRS data postulate that the volume FTAs are rational, which provides a new understanding about elements on the Moon.

Firstly, the statistical analysis indicates that the surfaces with TA $>$ 5 wt.% constitute less than 10% of the maria, while very-low-Ti ($<$1.5%) basalts are the most spatially abundant and high-Ti basalts are the least. This is comparable to the *LP* GRS results, but it is very different from the *Clementine* results. Also, the scatterplots of volume FA and TA indicate that the relationships between FA and TA are obviously linear before and after the threshold, 16 wt.% for FA.

Secondly, the volume FTAs in Maria Serentatis, Crisium, Moscoviense, Oceanus Procellarum and Apollo basin offer a new view about mare volcanism over the lunar surface. This is useful not only to pursue the source of mare basalts, but also to better understand volcanic processes in the important mare. The conclusion deserves to be further studied with more sources of data and even in-situ measurements by the *Yutu-2* rover in the current *CE-4* mission.

Thirdly, the comparisons between the CELMS, UV-VIS and *LP* GRS FTAs postulate that the FTAs in lunar regolith to some depth are different from those in the superficial layer. The results hint at the change of FTAs with depth and the complexity of lunar regolith in the vertical direction.

Finally, the low volume FTAs are widely distributed over almost the whole lunar highlands and in most patches of the SPA basin, which suggests that the lunar highlands crust is likely to be homogeneous at least in terms of the microwave thermophysical parameters.

Due to the limited number of samples and their spatial distribution, the inverted FTAs are not reliable at high latitude regions. With further exploration of the Moon, there will be more and more available input-output pairs for the BPNN network to improve the retrieval results. Also, several special features revealed by the volume FTAs are important for better understanding mare volcanism and mineral distributions on the Moon, which deserves to be further studied with more sources of data and even in-situ exploration.

Acknowledgements The LOLA data were downloaded from `http://pds-geosciences.wustl.edu/missions/lro/lola.htm`. The FeO and TiO_2 data derived from *Clementine* UV-VIS data and the *LP* GRS data were processed with the help of Prof. Wu Yunzhao from Purple Mountain Observatory, Chinese Academy of Sciences. This work was supported in part by the Key Research Program of the Chinese Academy of Sciences under Grant (XDPB11), in part by opening fund of State Key Laboratory of Lunar and Planetary Sciences (Macau University of Science and Technology) (Macau FDCT Grant No. 119/2017/A3), in part by the National Natural Science Foundation of China (Grant Nos. 41490633, 41371332 and 41802246) and in part by the Science and Technology Development Fund of Macau (Grant 0012/2018/A1). We wish to express our gratitude.

References

Adams, J. B., Head, J. W., McCord, T. B., Pieters, C., & Zisk, S. H. 1978, Geophys. Res. Lett., 5, 313

Cai, Z., & Lan, T. 2017, IEEE Transactions on Geoscience and Remote Sensing, 55, 5944

Chan, K. L., Tsang, K. T., Kong, B., & Zheng, Y.-C. 2010, Earth and Planetary Science Letters, 295, 287

Desai, A. J., Mohan, S., Kong, B., & Murty, S. 2014, Current Science, 824

Elphic, R. C., Lawrence, D. J., Feldman, W. C., et al. 2000, Journal of Geophysical Research, 105, 20333

Elphic, R. C., Lawrence, D. J., Feldman, W. C., et al. 2002, Journal of Geophysical Research (Planets), 107, 5024

England, A. W. 1975, Journal of Geophysical Research, 80, 4484

Fa, W., & Wieczorek, M. A. 2012, Icarus, 218, 771

Fang, T., & Fa, W. 2014, Icarus, 232, 34

Feldman, W. C., Gasnault, O., Maurice, S., et al. 2002, Journal of Geophysical Research (Planets), 107, 5016

Giguere, T. A., Taylor, G. J., Hawke, B. R., & Lucey, P. G. 2000, Meteoritics and Planetary Science, 35, 193

Gillis, J. J., Jolliff, B. L., & Korotev, R. L. 2004, Geochim. Cosmochim. Acta, 68, 3791

Haruyama, J., Ohtake, M., Matsunaga, T., et al. 2009, Science, 323, 905
He, L., Lang, L., Li, Q., & Zheng, W. 2013, Advances in Space Research, 51, 179
Heiken, G. H., Vaniman, D. T., & French, B. M. 1991, Lunar Sourcebook - A User's Guide to the Moon (Cambridge: Cambridge Univ. Press)
Hiesinger, H., Jaumann, R., Neukam, G., & Head, J. W. 2000, Journal of Geophysical Research, 105, 29239
Hu, G. P., Chan, K. L., Zheng, Y. C., & Xu, A. A. 2018, IEEE Transactions on Geoscience and Remote Sensing, 56, 5471
Jiang, J. S., & Jin, Y. Q. 2011, Selected Paper on Microwave Exploration of Lunar Surface in Chinese Chang'E-1 Project (Beijing: Science Press)
Jiang, J. S., Wang, Z. Z., & Li, Y. 2008, Engineering Sciences, 6, 16
Jin, Y. Q., F., Y., & Z., L. 2003, Chin J Radio Sci, 18, 477
Keihm, S. J. 1984, Icarus, 60, 568
Korokhin, V. V., Kaydash, V. G., Shkuratov, Y. G., Stankevich, D. G., & Mall, U. 2008, Planet. Space Sci., 56, 1063
Lawrence, D. J., Feldman, W. C., Barraclough, B. L., et al. 1998, Science, 281, 1484
Lawrence, D. J., Feldman, W. C., Elphic, R. C., et al. 2002, Journal of Geophysical Research (Planets), 107, 5130
Li, S., Li, L., Milliken, R., & Song, K. 2012, Icarus, 221, 208
Lippmann, R. P. 1987, IEEE Assp Magazine, 4, 4
Lucey, P. G., Blewett, D. T., & Hawke, B. R. 1998, Journal of Geophysical Research, 103, 3679
Lucey, P. G., Blewett, D. T., & Jolliff, B. L. 2000, Journal of Geophysical Research, 105, 20297
Matsunaga, T., Ohtake, M., Haruyama, J., et al. 2008, Geophysical Research Letters, 35, L23201
Mehra, P., & Wah, B. W. 1992, Artificial Neural Networks: Concepts and Theory (Los Alamitos, CA: IEEE Computer Society Press)
Meng, Z., Xu, Y., Zheng, Y., et al. 2014, Planet. Space Sci., 101, 1
Meng, Z., Yang, G., Ping, J., et al. 2016, Science China Earth Sciences, 59, 1498
Meng, Z. G., Zhao, R., Cai, Z. C., et al. 2017, IEEE Journal of Selected Topics in Applied Earth Observations and Remote Sensing, 10, 2984
Meng, Z. G., Hu, S., Wang, T. X., et al. 2018a, IEEE Journal of Selected Topics in Applied Earth Observations and Remote Sensing, 11, 3097
Meng, Z. G., Wang, H. H., Li, X. Y., et al. 2018b, International Archives of the Photogrammetry, Remote Sensing & Spatial Information Sciences, 42, 1279
Meng, Z. G., Wang, Q. S., Wang, H. H., Wang, T. X., & Cai, Z. C. 2018c, IEEE Journal of Selected Topics in Applied Earth Observations and Remote Sensing, 11, 3713
Meng, Z. G., Li, X. Y., Chen, S. B., et al. 2019, IEEE Journal of Selected Topics in Applied Earth Observations and Remote Sensing, 1 (DOI: 10.1109/JSTARS.2019.2892361)
Montopoli, M., di Carlofelice, A., Cicchinelli, M., et al. 2011, IEEE Transactions on Geoscience and Remote Sensing, 49, 3350
Morgan, G. A., Campbell, B. A., Campbell, D. B., et al. 2016, Journal of Geophysical Research (Planets), 121, 1498
Neal, C. R. 2009, Chemie der Erde / Geochemistry, 69, 3
Pabari, J. P. 2016, Planet. Space Sci., 132, 1
Pasckert, J. H., Hiesinger, H., & van der Bogert, C. H. 2018, Icarus, 299, 538
Pieters, C. 1993, in Remote Geochemical Analysis Elemental and Mineralogical Composition, 309
Pieters, C. M. 1999, Workshop on New Views of the Moon II: Understanding the Moon Through the Integration of Diverse Datasets
Pieters, C. M., Head, J. W., Isaacson, P., et al. 2008, Advances in Space Research, 42, 248
Pieters, C. M., Boardman, J., Buratti, B., et al. 2009, Current Science, 2009, 96(4), 500
Prettyman, T. H., Hagerty, J. J., Elphic, R. C., et al. 2006, Journal of Geophysical Research (Planets), 111, E12007
Rosenburg, M. A., Aharonson, O., Head, J. W., et al. 2011, Journal of Geophysical Research (Planets), 116, E02001
Rumelhart, D. E., & McClelland, J. L. 1987, Parallel Distributed Processing, Explotation in the Microstructure of Cognition – 1: Foundations (Cambridge: MIT Press)
Shkuratov, Y. G., Kaydash, V. G., & Opanasenko, N. V. 1999, Icarus, 137, 222
Spudis, P. D., & Sliz, M. U. 2016, in Lunar and Planetary Science Conference, 47, 1463
Spudis, P. D., & Sliz, M. U. 2017, Geophys. Res. Lett., 44, 1260
Tompkins, S., & Pieters, C. M. 1999, Meteoritics and Planetary Science, 34, 25
Wang, Z. Z., Li, Y., Zhang, D. H., et al. 2010, Science China Earth Sciences, 2010, 53(9), 1392
Wu, Y. 2012, Geochim. Cosmochim. Acta, 93, 214
Wu, Y., Li, L., Luo, X., et al. 2018, Icarus, 303, 67
Wu, Y., Xue, B., Zhao, B., et al. 2012, Journal of Geophysical Research (Planets), 117, E02001
Yan, B., Xiong, S. Q., Wu, Y., et al. 2012, Planet. Space Sci., 67, 119
Zhang, W., & Bowles, N. E. 2013, European Planetary Science Congress, 8, EPSC2013
Zheng, Y. C., Tsang, K. T., Chan, K. L., et al. 2012, Icarus, 219, 194